AIAA 2003-5054

The Bidirectional Vortex. Part 3: Multiple Solutions

A. B. Vyas and J. Majdalani
Marquette University
Milwaukee, WI 53233

M. J. Chiaverini
Space Center
Orbital Technologies Corporation (ORBITEC)
Madison, WI 53717

39th AIAA/ASME/SAE/ASEE Joint Propulsion Conference and Exhibit
20–23 July 2003
Huntsville, AL

39th AIAA/ASME/SAE/ASEE Joint Propulsion Conference and Exhibit
20-23 July 2003, Huntsville, Alabama

AIAA 2003-5054

The Bidirectional Vortex. Part 3: Multiple Solutions

Anand B. Vyas* and Joseph Majdalani†
Marquette University, Milwaukee, WI 53233
and
Martin J. Chiaverini‡
Orbital Technologies Corporation, Madison, WI 53717

The purpose of this article is to study the multi-directional vortex fields that can be engendered in a liquid-liquid thrust chamber driven by tangential gas injection. The work extends a former study whose focus on the fundamental mode of flow reversal has revealed a unique bidirectional flow. In the present article, we investigate the possible existence of multiple flow reversals which, in turn, can lead to multi-directional flows. The resulting flowfield will then consist of several co-axial spinning layers that remain separated by non-translating mantles. The multi-directional flow will hence comprise several sandwiched vortex tubes that switch axial direction across each mantle. Such multi-pass behavior has been recently observed in laboratory tests conducted at ORBITEC. In the current study the multiple solutions associated with each mode of flow reversal will be derived from Euler's equations.

Nomenclature

a = chamber radius
A_i = inlet area
b = chamber discharge radius
$b_{m,n}$ = radial distance to mantle location
d_e = discharge diameter
l = chamber aspect ratio, L/a
m = axial reversal mode number
n = integer indicating the order in a sequence
$\hat{\boldsymbol{n}}$ = unit vector normal to the surface
p = normalized pressure, $\overline{p}/(\rho U^2)$
p_0 = normalized pressure at the head end center
Δp = normalized pressure difference, $p - p_0$
$\overline{Q}_i$ = total inlet volumetric flow rate
Q_i = normalized volumetric flow rate, $\overline{Q}_i/(Ua^2) = \sigma^{-1}$
r = normalized radial coordinate, $\overline{r}/a$
S = empirical swirl number, $\frac{1}{2}\pi d_e a/A_i$
$\boldsymbol{u}$ = normalized velocity $(\overline{u}_r, \overline{u}_z, \overline{u}_\theta)/U$
U = mean inflow velocity, $\overline{u}_\theta(a, L)$
z = normalized axial coordinate, $\overline{z}/a$

β = normalized discharge radius, b/a
$\beta_{m,n}$ = nth radial fraction at the mth reversal mode

∇ = normalized del operator, $a\overline{\nabla}$
κ = inflow parameter, $Q_i/(2\pi l) = (2\pi\sigma l)^{-1}$
ν = kinematic viscosity, μ/ρ
ρ = density
σ = modified swirl number, $Q_i^{-1} = S/(\pi\beta)$

Subscripts
i = inlet property
r = radial component or partial derivative
z = axial component or partial derivative
θ = azimuthal component or partial derivative
= overbars denote dimensional variables

I. Introduction

IN a previous article by Vyas, Majdalani and Chiaverini,[1] the internal flow of a swirl-driven thrust chamber was analyzed. The particular chamber design allowed for flow entering upstream of the base to travel toward the head end, reverse direction while turning inwardly, and then cross the chamber length a second time while heading toward the nozzle. The specific features associated with the bidirectional flow motion are discussed at length in Ref. 1. The current investigation focuses on the higher flow reversal modes not considered previously.

The existence of a multi-directional flow has been suggested by recent test firings that utilize gaseous oxygen (GOX) injection. As shown in Fig. 1, a photograph taken at the end of the burn period of a

*Graduate student and Research Associate, Department of Mechanical and Industrial Engineering. Member AIAA.
†Assistant Professor, Department of Mechanical and Industrial Engineering. Member AIAA.
‡Lead Propulsion Engineer. Member AIAA.

Fig. 1 Grain contour after firing. Magnification reveals multiple grooves that may be caused by several coaxial vortex tubes.

swirl-driven, end burning combustor displays more than two concentric grooves in the head end cap. These grooves are appropriate of a recirculatory flow exhibiting multiple reversals. One possible explanation for this is that some of the reversed flow is actually turning at the base and spiraling outwardly from the center of the chamber. In this case, the flow will be spinning in the direction of gaseous injection at entry. A fraction of the oxygen may be spiraling along the bottom of the chamber and up to the head end in the central region where it meets the grain surface. The ensuing flowfield consists of two interwound spirals in the central region of the chamber, with one spinning upwardly, and the other spinning downwardly toward the nozzle. To the extent that this interesting behavior remains under investigation in hybrid and liquid rocket engines exhibiting bidirectional swirl, the current study attempts to illuminate the origin of multi-directional flows based on purely theoretical grounds.

To start, the earlier model used to predict the bidirectional flow polarity will be re-considered and shown mathematically to exhibit multiple discrete solutions. Subsequently, the attendant behavior will be characterized for several different mode numbers. Each mode will be shown to correspond to a given polarity level and, thereby, to a fixed number of mantles separating the now sandwiched vortex tubes.

In principle, the establishment of a multi-directional flow can have numerous advantages. It is well known, for example, that increasing the number of flow passes can prolong the particle residence time, improve the internal combustion efficiency, and increase the chemical energy release. Furthermore, the stacking of additional low temperature layers of propellant against the chamber sidewall is likely to provide a thicker and more resilient thermal barrier.

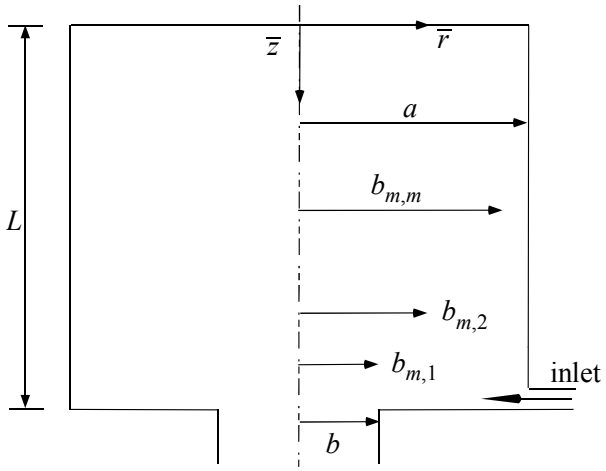

Fig. 2 Idealized chamber parameters.

Clearly, this multi-layered paneling can better protect the chamber wall from the hot combustion gases. Moreover, the reaction products can now be confined to the central core region in which mixing, centrifugal action, high speed rotation, and increased shear will result in a better conversion of chemical energy into mechanical work. Insofar as the built-in thermal protection enables us to be more flexible in material selection, it may also permit the use of thinner, lighter, and less expensive chamber walls. Additionally, the multiple particle passes will continue to increase the effective chamber length, thus leading to shorter engines. The advantages associated with a sandwiched flowfield in a multi-directional swirl-burner are clearly attractive despite the diverse questions that they raise. The current study will seek to provide some answers that can help to elucidate the observed flow patterns in laboratory experiments. It is also hoped that the multiple solutions to be described will be later exploited in developing advanced engine concepts that can secure the establishment of a technologically advanced, higher reversal mode configuration.

II. Mathematical Model

Our idealized chamber is modeled as a cylindrical tube of finite length L. The chamber is closed at the head end but left partially open at the downstream end where the chamber base is attached to one or several tubular nozzles. A sketch of the chamber is given in Fig. 2 where $\bar{r}$ and $\bar{z}$ are used to designate the radial and axial coordinates. The present study is focused on describing the flowfield in the portion of the chamber extending from the head end to the base. The fraction of the radius that is open to flow at the base is given by $\beta = \beta_0 = b/a$ and the chamber's aspect ratio is denoted by $l = L/a$. Additional radial fractions that will be later introduced are given by $\beta_{m,n} = b_{m,n}/a$

where $n = 1, 2, \ldots, m$. These fractions will be shown to delimit inner and outer radii of additional open areas that are physically required at higher flow reversal modes.

In the current model, the flow enters the chamber at $\bar{z} = L$ through one or more injection ports that only allow flow in the tangential direction. The solution domain is restricted to $0 \le \bar{z} \le L$, notwithstanding the thin Ekman layers and boundary layers that are formed along the endwalls and sidewalls, respectively.

A. Equations

The main focus here will be to investigate the inviscid behavior that can be used to mimic an actual flow at a large Reynolds number. For this reason, a standard set of assumptions is adopted according to which the flow remains (a) steady, (b) axisymmetric, (c) inviscid, (d) incompressible, (e) rotational, and (f) non-reactive. Furthermore, we normalize all spatial coordinates by the chamber radius a and all velocities by the average injection velocity U. Other variables are found in the Nomenclature. Under the stated assumptions, the mass and momentum conservation equations reduce to

$$\begin{cases} \nabla \cdot \boldsymbol{u} = 0 \\ \boldsymbol{u} \cdot \nabla \boldsymbol{u} = -\nabla p \end{cases} \tag{1}$$

By introducing the mean flow vorticity $\boldsymbol{\Omega} \equiv \nabla \times \boldsymbol{u}$, the vorticity transport equation can be used after taking the curl of Euler's equation. This operation begets

$$\nabla \times \boldsymbol{u} \times \boldsymbol{\Omega} = 0 \tag{2}$$

B. Boundary Conditions

The normalized boundary conditions that must accompany this simplified set can be attributed to: (i) a zero axial flow at the head end, (ii) a zero radial flow at the walls, (iii) symmetry about the centerline, (iv) a fully tangential inflow, and (v) an inflow that matches the outflow at the base. These auxiliary conditions are expressible by

$$\begin{cases} u_z(r,0) = 0; \;\; u_r(1,z) = 0; \; u_r(0,z) = 0 \\ u_\theta(1,l) = 1; Q_o = \int_0^{2\pi} \int_0^1 \boldsymbol{u} \cdot \hat{\boldsymbol{n}} \; r \mathrm{d}r \mathrm{d}\theta = Q_i \end{cases} \tag{3}$$

where $\boldsymbol{u} \cdot \hat{\boldsymbol{n}}$ represents the outflow velocity at the base.

III. Solution

Using parallel arguments to those presented by Vyas, Majdalani and Chiaverini,[1] a direct solution to the set above can be pursued. The analysis started by considering the $\theta-$ momentum equation, namely,

$$u_r \left(\frac{\partial u_\theta}{\partial r} + \frac{u_\theta}{r} \right) = 0 \tag{4}$$

By inspection, one may infer that, irrespective of u_r, the spin velocity takes the free vortex form

$$u_\theta = K / r \tag{5}$$

At the outset, the vorticity transport equation becomes

$$\frac{\partial (u_r \Omega_\theta)}{\partial r} - \frac{\partial (-u_z \Omega_\theta)}{\partial z} = 0 \tag{6}$$

where Ω_θ is the only non-zero vorticity component that is left in the absence of viscosity. At this juncture, one may follow Bloor and Ingham,[2] or Beran and Culick[3] and introduce the Stokes stream function ψ. In cylindrical coordinates, one can put

$$u_r = -\frac{1}{r}\frac{\partial \psi}{\partial z}; \quad u_z = \frac{1}{r}\frac{\partial \psi}{\partial r} \tag{7}$$

This transformation changes the vorticity transport equation into

$$-\frac{\partial \psi}{\partial z}\frac{\partial}{\partial r}\left(\frac{\Omega_\theta}{r}\right) + \frac{\partial \psi}{\partial r}\frac{\partial}{\partial z}\left(\frac{\Omega_\theta}{r}\right) = 0 \tag{8}$$

One family of solutions for Eq. (8) can be realized by choosing

$$\Omega_\theta = C^2 r \psi \tag{9}$$

This linear choice permits investigating explicit analytical solutions. At the outset, the vorticity equation turns into

$$\frac{\partial^2 \psi}{\partial z^2} + \frac{\partial^2 \psi}{\partial r^2} - \frac{1}{r}\frac{\partial \psi}{\partial r} + C^2 r^2 \psi = 0 \tag{10}$$

with

$$\frac{\partial \psi(r,0)}{\partial r} = 0 \;\; \text{(hard endwall)} \tag{11}$$

$$\frac{\partial \psi(1,z)}{\partial z} = 0 \;\; \text{(hard sidewall)} \tag{12}$$

$$\frac{\partial \psi(0,z)}{\partial z} = 0 \;\; \text{(axisymmetry)} \tag{13}$$

Proceeding with $\psi(r,z) = f(r)g(z)$, Eq. (10) can be decomposed into

$$-\frac{1}{g}\frac{\mathrm{d}^2 g}{\mathrm{d}z^2} = \frac{1}{f}\left(\frac{\mathrm{d}^2 f}{\mathrm{d}r^2} - \frac{1}{r}\frac{\mathrm{d}f}{\mathrm{d}r} + C^2 r^2 f\right) = \pm \lambda^2 \tag{14}$$

where λ is a separation constant. For $\lambda = 0$, the $z-$ equation yields $g(z) = K_1 z + K_2$ while the $r-$ equation turns into the familiar

$$\frac{\mathrm{d}^2 f}{\mathrm{d}r^2} - \frac{1}{r}\frac{\mathrm{d}f}{\mathrm{d}r} + C^2 r^2 f = 0 \tag{15}$$

whose solution can be expressed by

$$f(r) = K_3 \sin\left(\tfrac{1}{2} C r^2\right) + K_4 \cos\left(\tfrac{1}{2} C r^2\right) \tag{16}$$

The general form of the stream function becomes

$$\psi = \left(K_1 z + K_2\right)\left[K_3 \sin\left(\tfrac{1}{2}Cr^2\right) + K_4 \cos\left(\tfrac{1}{2}Cr^2\right)\right] \quad (17)$$

To find the unknown constants, application of the auxiliary conditions is necessary. Using Eq. (11), it can be inferred that $K_2 = 0$. Next, using Eq. (12), one obtains

$$K_1\left[K_3 \sin\left(\tfrac{1}{2}C\right) + K_4 \cos\left(\tfrac{1}{2}C\right)\right] = 0 \quad (18)$$

A. Solution Multiplicity

At this point, Eq. (13) can be used to set $u_r(0,z) = 0$ and, hence, $K_4 = 0$. At length, one is left with

$$K_1 K_3 \sin\left(\tfrac{1}{2}C\right) = 0 \quad (19)$$

From Eq. (19), it is clear that multiple exact solutions can exist for

$$C = 2m\pi; \quad m = 1,2,3,\ldots \quad (20)$$

where m represents the flow reversal mode number. For $m = 0$, one obtains the trivial problem for which flow reversal at the head end is prevented. The nontrivial patterns can be summarized through the use of

$$\psi = \kappa z \sin(m\pi r^2); \qquad \kappa = K_1 K_3 \quad (21)$$

Consequently, the velocity field can be expressed for each flow reversal mode number by writing

$$\boldsymbol{u} = -\frac{\kappa}{r}\sin(m\pi r^2)\boldsymbol{e}_r + \frac{K}{r}\boldsymbol{e}_\theta + 2\pi\kappa z\cos(m\pi r^2)\boldsymbol{e}_z \quad (22)$$

The next step is to determine the remaining constants, K and κ; this can be accomplished by invoking the last two conditions in Eq. (3).

First, the tangential inflow $u_\theta(1,l) = 1$ requires that $u_\theta(1,l) = K = 1$; hence,

$$K = 1 \quad (23)$$

Second, the remaining constant κ can be determined in a manner to accommodate a global mass balance. Accordingly, the mass flowing into the chamber must be discharged at the base through the ports of dimensionless radii $\beta_{m,n}$. Based on the form of u_z in Eq. (22), one can expect m internal mantles for a given flow reversal mode number m; the radial location of these mantles can be specified by

$$r = \beta_{m,n}; \quad n = 1,2,\ldots,m \quad (24)$$

Given a total inlet volumetric flow rate Q_i, one can put

$$2\pi\int_0^{\beta_{m,1}} \boldsymbol{u}\cdot\hat{\boldsymbol{n}}\, r\mathrm{d}r + 2\pi\int_{\beta_{m,2}}^{\beta_{m,3}} \boldsymbol{u}\cdot\hat{\boldsymbol{n}}\, r\mathrm{d}r + \ldots$$

$$+2\pi\int_{\beta_{m,n-1}}^{\beta_{m,n}} \boldsymbol{u}\cdot\hat{\boldsymbol{n}}\, r\mathrm{d}r + \ldots + 2\pi\int_{\beta_{m,m}}^{1} \boldsymbol{u}\cdot\hat{\boldsymbol{n}}\, r\mathrm{d}r = Q_i \quad (25)$$

Table 1 Matrix of mantle locations

m	$n=1$	$n=2$	$n=3$	$n=4$
1	$\beta_{1,1} = 1/\sqrt{2}$			
2	$\beta_{2,1} = 1/2$	$\beta_{2,2} = \sqrt{3}/2$		
3	$\beta_{3,1} = 1/\sqrt{6}$	$\beta_{3,2} = 1/\sqrt{2}$	$\beta_{3,3} = \sqrt{5/6}$	
4	$\beta_{4,1} = \sqrt{2}/4$	$\beta_{4,2} = \sqrt{6}/4$	$\beta_{4,3} = \sqrt{10}/4$	$\beta_{4,4} = \sqrt{14}/4$

where

$$\beta_{m,n} = \sqrt{(n-\tfrac{1}{2})/m}, \quad n = 1,2,3,\ldots,m \quad (26)$$

Equation (25) is obtained by ensuring that the inflow matches the outflow. It represents the total volumetric flow rate leaving the chamber at the nozzle exit. For $m = 1$, the single mantle associated with the classic bidirectional flow is recovered as $\beta_{1,1} = 1/\sqrt{2}$. For $m = 2$, two internal mantles emerge at

$$\beta_{2,1} = 1/2 \quad \text{and} \quad \beta_{2,2} = \sqrt{3}/2 \quad (27)$$

Because these locations delineate the radial distance at which flow polarity changes, they are listed in Table 1 for the first four flow reversal mode configurations.

B. Flow Characteristics

The radial location of the multiple mantles can be discerned graphically in the theoretical vector plots shown in Fig. 3 for $m = 2$ and 3. Streamlines corresponding to these vector plots are also shown in Fig. 4 for $m = 2$, 3 and 4. Both vector plots and streamline patterns suggest the possible co-existence of multidirectional flows with two or three passes spiraling co-axially within annular regions that span the length of the chamber. It may be speculated that a higher flow reversal configuration will require more energy to trigger and, hence, will form progressively at sufficiently large Reynolds numbers.

By virtue of $\hat{\boldsymbol{n}} = \boldsymbol{e}_z$, the mass balance equations for uni-, bi-, and tri-directional flowfields allow for the calculation of κ; one finds

$$\kappa = \frac{Q_i}{2\pi l} = \frac{1}{2\pi\sigma l} = \frac{A_i}{2\pi a L} \quad (28)$$

Note that κ is not expressed as function of the traditional, albeit empirical, swirl number S. When multidirectional flows are considered, the traditional swirl number S ceases to apply, being based on the product of the exit diameter and the chamber diameter. It becomes indeterminate in the presence of multiple exit diameters. Unsurprisingly, the modified swirl

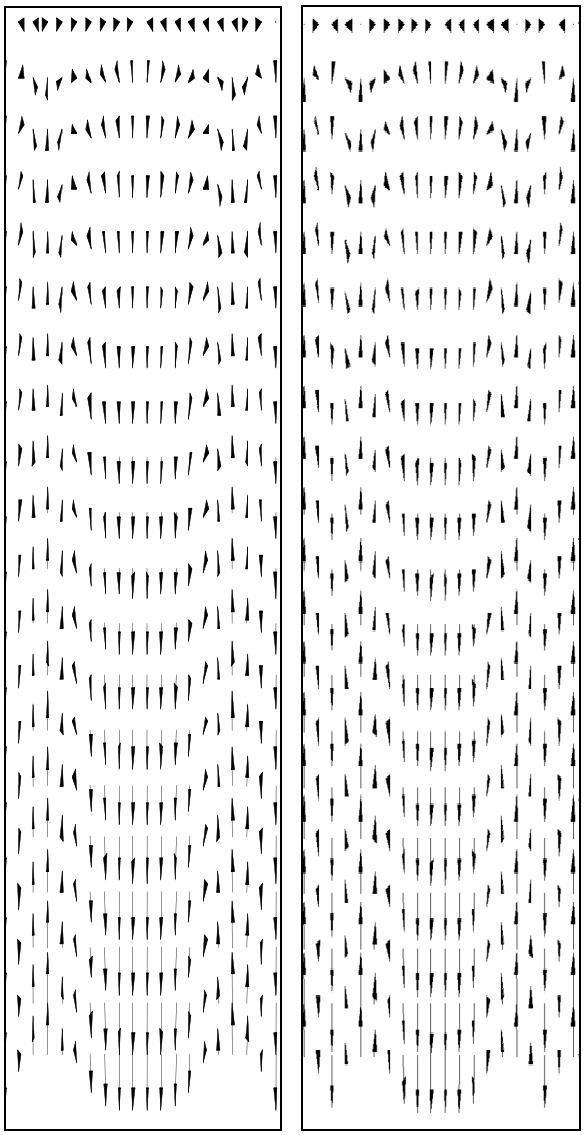

a) **b)**

Fig. 3 Vector plot at two flow reversal modes corresponding to a) $m = 2$ **and b)** 3 **.**

number σ continues to apply. This peculiar behavior may be attributed to the rigorous derivation of σ from the fundamental Euler equations. Essentially, σ is identified by the underlying physics to be the key similarity parameter –directly from the exact solution for this problem; S, on the other hand, does not stem from any existing exact or asymptotic solution. Historically, S was formerly posited, following careful rationalization, as a meaningful scaling parameter based on which useful empirical correlations could be developed. Despite their dissimilar origins, it is gratifying to see that S and σ differ by a constant when applied to the bidirectional flow.[1]

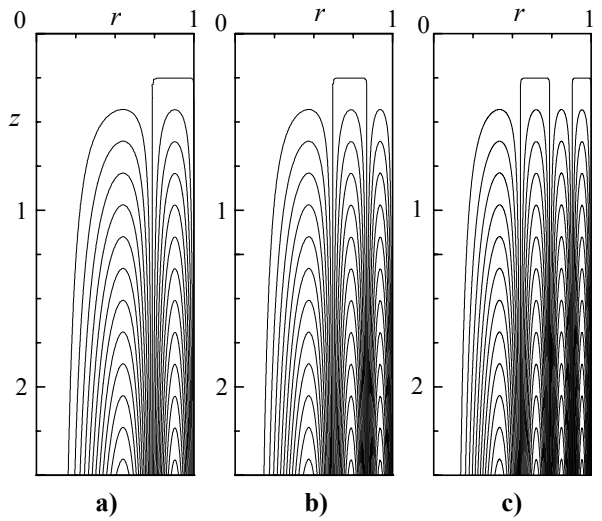

a) **b)** **c)**

Fig. 4 Streamlines for $l = \frac{5}{2}$ **and three reversal modes corresponding to a)** $m = 2$ **, b)** 3 **, and c)** 4 **.**

Having determined all the constants of integration, the multi-directional flowfield can be fully evaluated. We now have

$$\psi = \kappa z \sin(m\pi r^2) = \frac{1}{2\pi\sigma}\frac{z}{l}\sin(m\pi r^2) \qquad (29)$$

in conjunction with

$$\boldsymbol{u} = -\frac{\kappa \sin(m\pi r^2)}{r}\boldsymbol{e}_r + \frac{1}{r}\boldsymbol{e}_\theta + 2\pi m\kappa z \cos(m\pi r^2)\boldsymbol{e}_z$$

$$= -\frac{1}{2\pi\sigma l}\frac{\sin(m\pi r^2)}{r}\boldsymbol{e}_r + \frac{1}{r}\boldsymbol{e}_\theta + \frac{mz\cos(m\pi r^2)}{\sigma l}\boldsymbol{e}_z \qquad (30)$$

Plots of the axial and radial velocity distributions are furnished in Fig. 5 for the first four flow reversal mode numbers. In Fig. 5a, it can be seen that the number of zero crossings marked by the axial velocity curves coincides precisely with the flow reversal mode number. Clearly, the intersections of the u_z curves with the zero axis delineate regions of opposing axial flow. As the mode number is increased, the radial location of the first mantle moves closer to the core. For the first four modes, one finds

$$\beta_{m,1} = \{0.707, 0.5, 0.408, 0.3535\}\ ;\ m = 1,2,3,4 \qquad (31)$$

Conversely, the last point of flow reversal moves closer to the sidewall with each successive increase in m. One enumerates

$$\beta_{m,m} = \{0.707, 0.866, 0.913, 0.935\}\ ;\ m = 1,2,3,4 \qquad (32)$$

It should be noted that, whenever m is quadrupled, the radial distance to the first internal mantle is halved. This result can be inferred from Eq. (26).

Figure 5a clearly indicates that, for odd values of m, the outermost vortex first spirals upwardly,

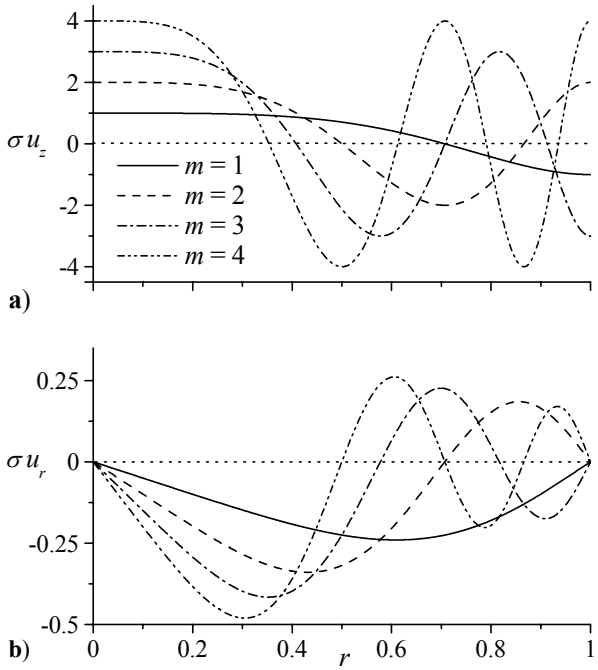

Fig. 5 Axial and radial velocity distributions along the chamber radius for the first four flow reversal modes. The axial velocity is plotted at the base.

reverses at the head end, and then returns to the base. The same reversal process is repeated at the base at progressively higher mode numbers. The results so obtained seem to concur well with the recent experimental and numerical findings of Anderson and co-workers[4] see Table 2). However, the set of operating conditions that begets the onset of multiple mantles is still a subject of investigation. The existence of positive radial velocity in Fig. 5b suggests that, for a sandwiched layer, both outward and inward cross flows are possible in the radial direction. This can be attributed to the fact that cross flow can originate from both the outer and inner vortex tubes that surround a given sandwiched layer.

Figure 5 also indicates that, for even mode numbers, the outermost vortex will be directed toward the nozzle. In practice, securing such a flow reversal pattern may require the addition of secondary outlet sections at the base. In spite of being theoretically plausible, the existence of $m-1$ outflow segments along the base may require additional outlet partitions that may be difficult to implement. From a practical standpoint, such partitions are likely to involve complex manifolding whose detail requires further inquiry.

Table 2 Comparison to the results of Anderson and co-workers[4] (2003)

β_{exp}	β_{analytic}	β_{CFD}	$\lvert\beta_{\text{analytic}}-\beta_{\text{exp}}\rvert$	$\lvert\beta_{\text{CFD}}-\beta_{\text{exp}}\rvert$
0.296	0.354	0.305	0.058	0.009
0.594	0.612	0.385	0.018	0.209
0.803	0.791	0.787	0.012	0.016
0.955	0.935	1.000	0.020	0.045

C. Pressure Field

Having exacted the velocity field, the pressure gradients in the radial and axial directions can be obtained as well. From Eq. (1), one finds

$$\frac{\partial p}{\partial r}=\frac{1}{r^3}\left\{1+\kappa^2\left[\sin^2(m\pi r^2)-m\pi r^2\sin(2\pi r^2)\right]\right\} \quad (33)$$

and

$$\frac{\partial p}{\partial z}=-4\pi^2m^2\kappa^2z \quad (34)$$

Note that the radial pressure gradient is very weakly sensitive to the flow reversal mode configuration number. At leading order, it is inversely proportional to the cubic distance from the core. From Eq. (33), it is clear that

$$\frac{\partial p}{\partial r}=\frac{1}{r^3}\left[1+O\left(\kappa^2\right)\right] \quad (35)$$

This behavior is identical to the one exhibited by the single mantle case. The difference here is that the axial pressure gradient along the centerline increases at higher mode numbers. It rises from $-4\pi^2\kappa^2z$ at $m=1$ to $-16\pi^2\kappa^2z$ at $m=2$.

Having determined the pressure gradients, the actual pressure drop along the length of the chamber can be immediately evaluated by partial integration of Eqs. (33)–(34). This operation yields

$$\Delta p=-\frac{1}{2r^2}\left\{1+\tfrac{1}{2}\kappa^2\left[8m^2\pi^2r^2z^2+1-\cos(2m\pi r^2)\right]\right\} \quad (36)$$

where $\Delta p=p-p_0$ represents the pressure referenced to the core value at the head end. For $m=1$, one recovers the result obtained by Vyas, Majdalani and Chiaverini.[1] As in the case of a single mantle, the pressure drop appears to be weakly dependent on the flow reversal mode number. Due to the small size of κ, one can put

Table 3 Internal zeros of vorticity and radial speed

m	$j=1$	$j=2$	$j=3$	$j=4$
1	– –			
2	$\gamma_{1,1}=1/\sqrt{2}$			
3	$\gamma_{2,1}=1/\sqrt{3}$	$\gamma_{2,2}=\sqrt{2/3}$		
4	$\gamma_{3,1}=1/2$	$\gamma_{3,2}=1/\sqrt{2}$	$\gamma_{3,3}=\sqrt{3}/2$	
5	$\gamma_{4,1}=1/\sqrt{5}$	$\gamma_{4,2}=\sqrt{2/5}$	$\gamma_{4,3}=\sqrt{3/5}$	$\gamma_{4,4}=2/\sqrt{5}$

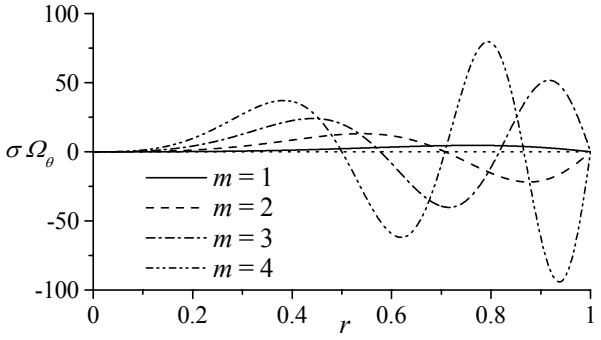

Fig. 6 Tangential vorticity distribution along the chamber radius for the first four flow reversal modes.

$$\Delta p = -\frac{1}{2r^2}\left[1+O\left(\kappa^2\right)\right] - 2m^2\pi^2\kappa^2 z^2 \qquad (37)$$

Equation (37) indicates that the quadratic dependence on z can become appreciable at high flow reversal mode numbers. In practice, it remains of marginal importance due to the small size of $m^2\kappa^2$ at realistically low mode numbers .

D. Vorticity Field

Vorticity can be similarly calculated. One obtains

$$\Omega_\theta = \frac{\partial u_r}{\partial z} - \frac{\partial u_z}{\partial r} = 4m\pi^2\kappa r z \sin(m\pi r^2) \qquad (38)$$

As shown in Fig. 6, the vorticity vector switches sign while sweeping radially from one flow region to another. Both radial velocity and vorticity vanish along the centerline and the sidewall; they change their sense of direction when $r=\gamma$ and $m\pi\gamma^2 = j\pi$ where $j=1,2,\ldots,m-1$. The corresponding zeros may be obtained from

$$\gamma_{m-1,j} = \sqrt{j/m}\ ;\ j=1,2,\ldots,m-1\ ,\ m=2,3,\ldots \qquad (39)$$

The points of zero vorticity and radial velocity are given in Table 3 for the first five flow reversal mode numbers.

IV. Conclusions

Based on theoretical considerations, a multi-directional flow solution is shown to exist inside an idealized, swirl-driven thrust chamber. The multi-directional flow satisfies the steady Euler equations and their attendant boundary conditions. For a given flow reversal mode number, an identical number of internal mantles is observed. These mantles subdivide the chamber volume into axisymmetric annuli in which coaxial vortex tubes are established. These vortex tubes switch axial direction as the radial distance is increased. At higher flow reversal modes, the innermost mantle shifts toward the chamber axis while the outermost moves closer to the sidewall. The complex patterns evolving at higher modes may be difficult to reproduce physically. Nonetheless, their theoretical existence lends support to recent tests in which multiple annular flows were reported. Due to the increased efficiency and desirable heat transfer characteristics associated with multi-layering, it is hoped that the solutions presented here be further explored in physical applications involving swirl burners, cyclonic separators, and other vortex driven flows.

Acknowledgments

The first two authors gratefully acknowledge the support received from NASA and the Wisconsin Space Grant Consortium. The authors also wish to thank William H. Knuth, Ronald R. Teeter, and Eric E. Rice of Orbital Technologies Corporation; their additional support is greatly appreciated.

References

[1]Vyas, A. B., Majdalani, J., and Chiaverini, M. J., "The Bidirectional Vortex. Part 1: An Exact Inviscid Solution," AIAA Paper 2003-5052, July 2003.

[2]Bloor, M. I. G., and Ingham, D. B., "The Flow in Industrial Cyclones," *Journal of Fluid Mechanics,* Vol. 178, 1987, pp. 507-519.

[3]Beran, P. S., and Culick, F. E. C., "The Role of Non-Uniqueness in the Development of Vortex Breakdown in Tubes," *Journal of Fluid Mechanics,* Vol. 242, 1992, pp. 491-527.

[4]Anderson, M., Valenzuela, R., Rom, C., Bonazza, R., and Chiaverini, M. J., "Vortex Chamber Flow Field Characterization for Gelled Propellant Combustor Applications," AIAA Paper AIAA 2003-4474, July 2003.